Lightweight Unmanned Aerial Vehicle and Structure-from-Motion Photogrammetry for Generating Digital Surface Model for Open-Pit Coal Mine Area and Its Accuracy Assessment

Dieu Tien Bui[1(✉)], Nguyen Quoc Long[2], Xuan-Nam Bui[3], Viet-Nghia Nguyen[2], Chung Van Pham[2], Canh Van Le[2], Phuong-Thao Thi Ngo[4], Dung Tien Bui[5], and Bjørn Kristoffersen[1]

[1] GIS and IT Group, Department of Business and IT, University College of Southeast Norway, Gullbringvegen 36, 3800 Bø i Telemark, Norway
Dieu.T.Bui@usn.no
[2] Department of Mine Surveying, Hanoi University of Mining and Geology, Hanoi, Vietnam
Nguyenquoclong@humg.edu.vn
[3] Faculty of Mining, Hanoi University of Mining and Geology, Hanoi, Vietnam
Buixuannam@humg.edu.vn
[4] Faculty of Information Technology, Hanoi University of Mining and Geology, Hanoi, Vietnam
Ngothiphuongthao@humg.edu.vn
[5] Center for the Development of Science and Technology, Hanoi University of Mining and Geology, Hanoi, Vietnam
BuiTienDung204@gmail.com

Abstract. Recent technological innovations have led to the available of lightweight Unmanned Aerial Vehicle (UAV) and Structure-from-Motion (SfM) photogrammetry that are successfully applied for 3D topographic surveys. However, application of UAV and SfM for complex topographic areas i.e. open-pit mine areas is still poorly understood. This paper aims to investigate and verify potential application of these techniques for generating Digital Surface Model (DSM) at open-pit coal mine area and assessing its accuracy. For this purpose, the Nui Beo open-pit coal mine located in northeast Vietnam is selected as a case study. Accordingly, a total of 206 photos were captured using DJI Phantom 3 Professional. In addition, 19 ground control points (GCPs) were established using Leica TS09 total station. The accuracy of DSM was assessed using root-mean-square error (RMSE) in X, Y, Z, XY, and XYZ components. The result showed that the DSM model has high accuracy, RMSE on the 12 calibrated GCPs for X, Y, Z, XY, XYZ is 1.1 cm, 1.9 cm, 0.8 cm, 2.2 cm, and 2.3 cm, respectively, whereas RMSE on the 7 checked GCPs is 1.8 cm, 2.4 cm, 3.2 cm, 3.0 cm, and 4.4 cm for X, Y, Z, XY, XYZ components, respectively. We concluded that small UAV and SfM are feasible and valid tools for 3D topographic mapping in complex terrains such as open-pit coal mine areas.

D. Tien Bui et al. (eds.), *Advances and Applications in Geospatial Technology and Earth Resources*, https://doi.org/10.1007/978-3-319-68240-2_2

Keywords: UAV · Structure-from-Motion · Photogrammetry · Open-pit mine · Nui Beo · Quang Ninh · Vietnam

1 Introduction

Direct surveying techniques i.e. Electronic Distance Measurement (EDM) surveys or Total Station (TS) and RTK Global Navigation Satellite System (GNSS) are the most widely used in surveying engineering and volumetric computation at open pit mining due to ability to obtain observations with millimeter accuracy [1]. However, they are cost and time consuming techniques, and in some complex environments, these techniques may be unsafe to workers [2]. Recent technological innovations have provided new alternative techniques for topographic surveying such as Terrestrial Laser Scanning (TLS) and airborne Light Detection and Ranging (LiDAR) or airborne laser scanning (ALS).

For TLS, although this technique is quite straightforward to use and millimeter accuracy could be obtained for objects at short distances, the cost and survey time still are a critical issue because this technique requires many scanning stations. Therefore, TLS may not be suited in projects dealing with complex topographies such as open-pit mines [3]. Regarding LiDAR, the accuracy is heavily influenced by GNSS and Inertial Measurement Unit (IMU) systems. Although accuracy is reported 0.1–0.5 m for vertical and 0.1–0.5 m for horizontal, however, higher vertical errors could occur in areas with complex environments [4].

Recent advancements in robots and GNSS technologies have provided various Unmanned Aerial Vehicles (UAVs) that can be used for topographic surveying. Especially, small and low-cost UAVs with nonmetric digital cameras are becoming a valid and effective alternative surveying technique for topographic reconnaissance and volumetric computation. In addition, the fusion of computer vision and photogrammetry have provided various Structure-from-Motion (SfM) and Multi-View Stereo (MVS) algorithms that have been successfully used for automatic processing UAV images with high quality results [5].

Overall, the main advantage of lightweight UAVs is that they can fly at low altitude with slow speed providing captured photos with fine spatial resolution and users defined temporal resolutions. The SfM algorithms are capable to automatically process orientation and geometry of images as well as camera positions [6]. More specifically, these algorithms have included MVS techniques that enable us to generate various 3D productions from UAV overlapped images, i.e. 3D point cloud and Digital Surface Model (DSM). Consequently, UAV and SfM photogrammetry have successfully been used in various fields i.e. surveying earthwork projects [2], stockpile volumetric [7], topography reconstructions [8], gravel-pit surveying and change estimation [9], ice-cored moraine degradation [10], erosion monitoring [11], precision farming applications [12], and geological mapping [13]. Common conclusions from these works demonstrate that UAV and SfM are new and efficient tools. Nevertheless, accuracy of the topographic mapping and its generated DSM derived from small UAVs and SfM photogrammetry at open pit mines has been rarely assessed and is still poorly understood.

In this work, we extend the body of knowledge by assessing the utility of UAV and SfM photogrammetry for topographic mapping and DSM at complex terrain of open-pit coal mine, with a case study at the Nui Beo coal mine in Quang Ninh province (Vietnam). Accordingly, a DJI Phantom 3 Professional was used to capture images, whereas ground control points were measured by using a Leica TS09 total station. The image processing was carried out using Agisoft®PhotoScan Professional 1.0 (APP). Finally, accuracy assessment was performed and conclusions are given.

2 Materials and Methods

2.1 Study Site

The study area (Fig. 1) is the Nui Beo open-pit coal mine (107°7'46", 20°57'46"), one of the five largest open-cast mines in Vietnam (Nui Beo, Deo Nai, Ha Tu, Cao Son, and Coc Sau), located in the Ha Long city, Quang Ninh province (Vietnam), around 160 km east of the Hanoi city. This mine is operated by the Nui Beo coal joint stock company that belongs to Vietnam National Coal and Mineral Industries (VINACOMIN) group.

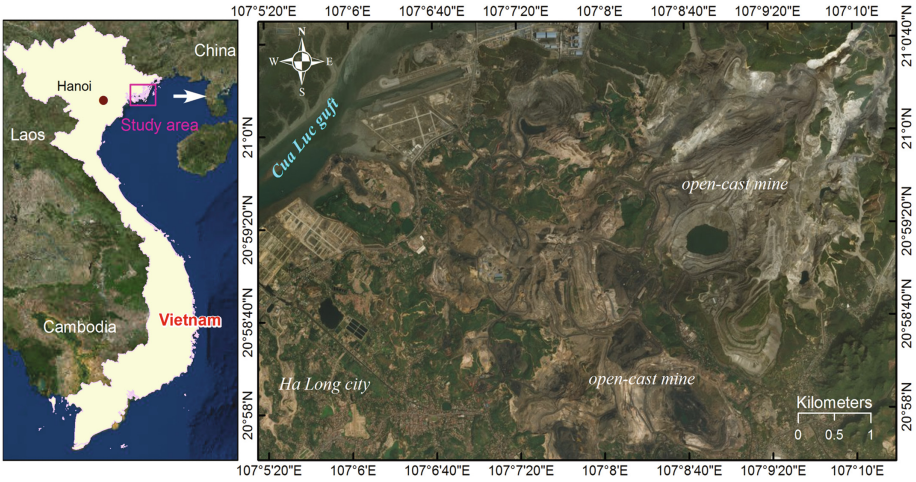

Fig. 1. Location of the Nui Beo coal mine.

It is noted that the Quang Ninh province produces 100% exported coals and nearly 90% domestic coals in Vietnam. The Nui Beo open-pit coal mine was designed in 1983 by the Giproruda Institute (former Soviet Union) and has officially operated since May 19, 1989. Total coal production is estimated around 32 million tons [14]. Total mineral coal area is around 3.75 km^2 for the open-pit coal mines and 5.6 km^2 for the underground coal mine.

Topographically, the Nui Beo coal mine presents complicated terrain conditions where the center is the opencast mining area, whereas the opening landfill is in the

north, industrial works locates in the south, and in the west is waste dumps and mining pits. Due to the surface mining activities, the high-end exploitation level reached −250 m (Fig. 2) [15].

Fig. 2. A photo of the Nui Beo open-pit coal mine (the photo was taken by Viet-Nghia Nguyen on January 6, 2017).

2.2 UAV and Camera

In this work, a lightweight DJI Phantom 3 professional (Fig. 3), which has been widely used for small surveying projects, was used to capture images due to its small size and weight, low-cost, ease of use, and still provides good image quality. This is a rotary wing quadcopter drone with four powerful motors that enable it to have high resistance wind and air pressure as well as higher stability [16]. The weight of the drone is approximately 1.3 kg including 0.75 kg payload. Flight time can reach 23 min with maximum speed 16 m/s in the no wind condition, whereas the highest altitude the drone can fly is 6 km [17].

The drone is equipped by nonmetric RGB Sony EXMOR camera with focal length is 3.61 mm and sensor size is 4.72 × 6.3 mm. This is called 4 K resolution camera (FC300X) where each image has a resolution of 4000 × 3000 pixels. Detailed characteristics of the DJI Phantom 3 professional and Sony EXMOR camera are summarized in Table 1.

Table 1. Characteristics of the DJI Phantom 3 professional and Sony EXMOR camera used in this research.

No.	Parameter	Characteristics
1	Total weight	1.28 kg
2	Height, length, width	18.5 cm, 28.9 cm, 28.95 cm
3	GNSS	GPS/GLONASS
4	Max. flight altitude	6 km
5	Max. flight time	~23 min
6	Max. speed	16 m/s
7	Operating temperature	0°C to 40°C
8	Camera sensor	Sony EXMOR 1/2.3", total pixels is 12.76 M
9	Camera lens	FOV 94° 20 mm f/2.8
10	Electronic shutter speed	8 s–1/8000 s
11	Image format	DNG, JPEG
12	Stabilization	3-axis (pitch, roll, yaw)

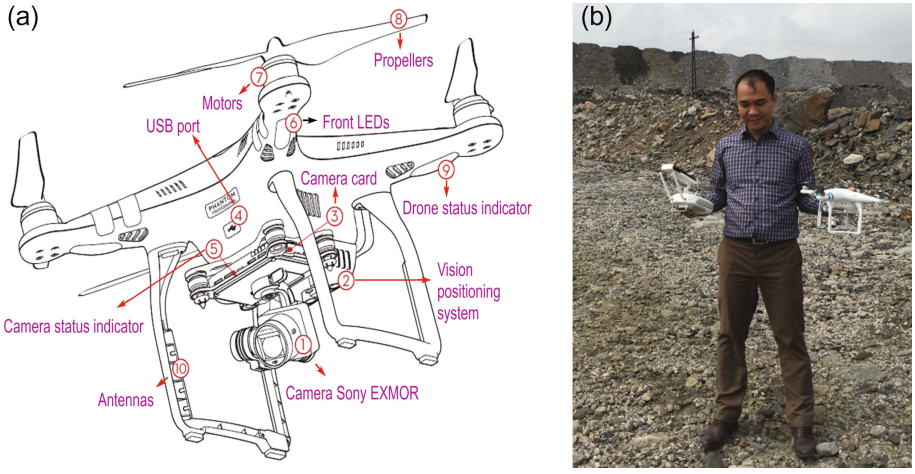

Fig. 3. (a) Description of components of a DJI Phantom 3 Professional (source http://www.dji.com/phantom-3-pro); (b) photo of a surveyor (Long-Quoc Nguyen) with the DJI Phantom 3 Professional used in this research.

2.3 Establishment of Ground Control Point

Before the image acquisition was carried out, it was necessary to place Ground Control Points (GCPs) for the study area surface. These GCPs are used for geo-referencing and evaluating the accuracy of the DSM model. Because the Nui Beo open-pit coal mine still is operating, field reconnaissance was conducted to select safe areas for placing these GCPs with a help of a handhold GPS i.e. iGeotrans [18] installed in iPhone 5. Accordingly, a total of 19 GCPs was established for a test area of 0.22 km^2 at the Nui Beo open-pit coal mine.

The GCPs were marked with a highly reflective material for enhancing the contrast in order for easier detecting in resulting images (Fig. 4a). The radius of the reflective material of 20 cm was used. In the next step, coordinates (x, y, z) for these GCPs were determined using a Leica TS09 total station (angular accuracy is 1" and distance accuracy is 1.5 mm + 2 ppm) and the available horizontal and vertical surveying network at the mine area. The measured coordinates (VN2000/UTM Zone 48 N) for these GCPs are shown in Table 2.

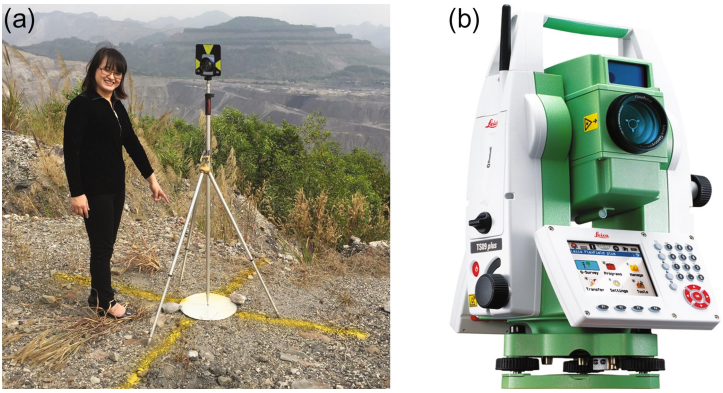

Fig. 4. (a) an example of established GCP and (b) Leica TS09 total station used for this work.

Table 2. XYZ coordinates of the Ground Control Points (GCPs) that measured by Leica TS06 total station for this study.

No.	Ground control point	X (m)	Y (m)	Z (m)
1	GCP1	722231.775	2319835.279	−42.683
2	GCP2	722175.977	2319988.738	−59.962
3	GCP3	722165.175	2320077.164	−69.634
4	GCP4	722148.859	2320112.948	−70.424
5	GCP5	722182.790	2320125.694	−74.195
6	GCP6	722325.858	2319730.317	−14.197
7	GCP7	722238.322	2319680.871	−5.625
8	GCP8	722150.193	2319657.720	3.110
9	GCP9	722198.746	2319720.943	−19.339
10	GCP10	722185.584	2319749.567	−20.668
11	GCP11	722152.108	2319776.945	−12.034
12	GCP12	722133.557	2319809.538	−7.448
13	GCP13	722122.263	2319871.090	−8.017
14	GCP14	722081.792	2319920.477	−7.439
15	GCP15	722076.996	2319993.553	−9.211
16	GCP16	721805.884	2319980.605	134.184
17	GCP17	721840.646	2319945.641	126.022
18	GCP18	721814.051	2319902.623	134.604
19	GCP19	721818.550	2319864.493	134.583

2.4 Image Acquisition

To design the flight plan, Pix4DCapture application installed in an Apple tablet was used. Accordingly, endlap and sidelap of images were selected as 80%. The application configured the flights, and then, the result was uploaded to the DJI Phantom 3 professional via telemetry. Due to the very high variation of the topography, a flying altitude of 90 m was selected and the flying speed was around 5 m/s. The auto and navigation modes were used for the flight project, and during flight, the drone could adjust its position and camera orientation automatically to ensure consistent images. As result, a total of 206 images were captured and used for deriving DSM. These images covered an area of 0.22 km^2.

When the flight project was done, these captured images were transferred from the drone into a personal computer for SfM analyses established in the Agisoft® PhotoScan Professional (APP). This photogrammetric software was used because it has proven to outperform other softwares in terms of accuracy [19]. Accordingly, the overall goal of the SfM analyses was to produce a high accurate and precise DSM for the project.

2.5 Photogrammetric Processing

Typically, the image processing using the SfM procedure consists of five steps: (i) photo alignment; (ii) bundle block adjustment; (iii) optimization, (iv) 3D surface reconstruction, (v) generation of Digital Surface Model (DSM).

In the first step, the captured images were aligned though a process named as selecting and triangulating the photos, also called "photo alignment". Using the function of "image quality" in APP, images with quality less than 0.5 were filtered and eliminated to ensure the high quality of the final 3D point cloud and the DSM models [20]. Position of these images that were initially estimated using the GNSS geographical coordinates was converted to the projected coordinate system (VN2000). Coordinates of these images were optimized in later processes. Feature detection process that used the Scale Invariant Feature Transform (SIFT) algorithm [21] was then carried out to detect tie points (also called key points) from overlapping areas (at least from 3 images), and in addition, other point across the body of images were also detected. These tie points and these GCPs were used later for the image matching and determining image and camera geometries.

Table 3. Camera-lens parameters used for this research.

No.	Parameter	Explanation
1	f	Focal length
2	Cx, Cy	Principal point offset of the image in x and y image coordinates
3	$K_1, K_2, K_3,$ and K_4	Radial distortion coefficient of $2^{nd,}$ 4^{th}, 6^{th}, 8^{th} -order, respectively
4	$P_1, P_2, P_3,$ and P_4	Tangential distortion coefficient
5	B_1 and B_2	Affinity and skew coefficients

In the second step, determination of the internal and external orientation parameters of the camera (including 13 parameters in Table 3) was carried out using these tie points and the GCPs, available information of the focal length and the camera parameters on the captured images, and the Camera Calibration tool in the APP software. Accordingly, the camera locations were determined using the greedy algorithm, and then, the camera positions, their orientation, and their distortion parameters were updated and adjusted via the bundle block adjustment process.

It is noted the RGB Sony EXMOR used in this study is frame type camera, therefore the calibration process was performed using the Brown's distortion model [22] to transform point coordinates in the local camera (X, Y, Z) to pixel coordinates (u, v) in the image frame using Eqs. 1, 2, 3 [23] as follows:

$$x^{'} = x(1 + K_1r^2 + K_2r^4 + K_3r^6 + K_4r^8) + (P_1(r^2 + 2x^2) + 2P_2xy)(1 + P_3r^2 + P_4r^4) \quad (1)$$

$$y' = y(1 + K_1r^2 + K_2r^4 + K_3r^6 + K_4r^8) + (P_2(r^2 + 2y^2) + 2P_2xy)(1 + P_3r^2 + P_4r^4) \quad (2)$$

$$u = 0.5 * w + Cx + x'f + x'B_1 + y'B_2;\ v = 0.5 * h + Cy + y'f \quad (3)$$

where $x = X/Z$; $y = Y/Z$; r = sqrt $(x^2 + y^2)$; w, h are the width and the height of the image in pixels; x', y' are the projected coordinates in the image plane; and u, v are pixel coordinates in the image frame.

Should be pointed out that although the internal and external parameters of the camera were found, however, in some cases, resulting DSM models may still show significant errors due to topographic complexity of the project and outliers points [20]. Therefore, an optimization process in step 3 was carried out. Accordingly, the tie points were manually inspected and outliers were removed. In addition, the number of GCPs was adjusted for possibly minimizing RMSE.

Once the optimization process was done and the optimized camera positions were derived, a dense surface reconstruction was carried out, in which depth maps for all the images were computed and combined, to generate 3D dense point cloud. Accordingly, the Mild depth filtering algorithm was adopted due to ability to eliminate outliers but still keep important features. This algorithm has proven suitable for poorly textured roofs areas [23], such as open-cash coal mine. Finally, the 3D dense point cloud was used to generate the final DSM for the study area.

2.6 Accuracy Assessment

Accuracy assessment of the Digital Surface Model (DSM) is an important task, and without this task, the DSM is useless. In this project, both the horizontal and vertical assessments were carried out by comparing DSM with the GCPs measured by the Leica total station in term of Root Mean Square Error (RMSE). More specifically, assessments in easting ($RMSE_X$), northing ($RMSE_Y$), vertical ($RMSE_Z$), horizontal

($RMSE_{XY}$), and all components ($RMSE_{XYZ}$) were used, as suggested in Agüera-Vega [24], using equations as follows:

$$RMSE_{\mathrm{X}} = SQRT\left[(1/n)\sum_{i=1}^{n}(X_{\mathrm{DSM}} - X_{\mathrm{GCPi}})^2\right] \quad (4)$$

$$RMSE_{\mathrm{Y}} = SQRT\left[(1/n)\sum_{i=1}^{n}(Y_{\mathrm{DSM}} - Y_{\mathrm{GCPi}})^2\right] \quad (5)$$

$$RMSE_{\mathrm{Z}} = SQRT\left[(1/n)\sum_{i=1}^{n}(Z_{\mathrm{DSM}} - Z_{\mathrm{GCPi}})^2\right] \quad (6)$$

$$RMSE_{\mathrm{XY}} = SQRT\left[(1/n)\sum_{i=1}^{n}((X_{\mathrm{DSM}} - X_{\mathrm{GCPi}})^2 + (Y_{\mathrm{DSM}} - Y_{\mathrm{GCPi}})^2)\right] \quad (7)$$

$$RMSE_{\mathrm{XYZ}} = SQRT\left[(1/n)\sum_{i=1}^{n}((X_{\mathrm{DSM}} - X_{\mathrm{GCPi}})^2 + (Y_{\mathrm{DSM}} - Y_{\mathrm{GCPi}})^2 + (Z_{\mathrm{DSM}} - Z_{\mathrm{GCPi}})^2)\right] \quad (8)$$

where X_{GCPi} and X_{DSM} are the X-coordinate component of GCP and corresponding coordinate in DSM, respectively; Y_{GCPi} and Y_{DSM} are the Y-coordinate component of GCP and corresponding coordinate in DSM, respectively; Z_{GCPi} and Z_{DSM} are the Z-coordinate component of GCP and corresponding coordinate in DSM, respectively.

3 Results and Discussion

3.1 Digital Surface Model and Its Accuracy

To determine the best camera-lens parameters in this research, an optimization process was carried out. For this task, the 19 GCPs were split in two subsets: (i) the first one is a calibrating dataset that accounts for 70% (12 GCPs) of the total GCPs and were used for the calibration of the camera-lens model and the bundle adjustment; the second one is a checking dataset that consists of the remaining GCPs (30%, 7 GCPs) were used for checking the final model and confirming it accuracy. Distribution of these GCPs in this study area is shown in Fig. 5. It could be seen that no GCP was placed at the lower left corner and the central of the study areas. This is because these were unsafe areas to reach due to the coal seams still were exploiting.

Using the detected tie points and 13 GCPs (Fig. 5), the optimization process was carried out with five runs to ensure a stable result. The final calibrated coefficients of the camera-lens model are shown in Table 4. It could be seen that the errors of these parameters are low, indicating good results.

Table 4. Camera-lens calibrated coefficients.

No	Parameter	Value	Error
1	f	2314.550	0.59
2	Cx	−22.8598	0.1600
3	Cy	11.4502	0.1000
4	B1	9.0365	0.2700
5	B2	2.7214	0.1500
6	K1	−0.006685	0.000110
7	K2	−0.008707	0.000390
8	K3	0.035100	0.000540
9	K4	−0.016010	0.000250
10	P1	−0.001735	0.000024
11	P2	0.000523	0.000009
12	P3	−0.767175	0.013000
13	P4	0.264946	0.008700

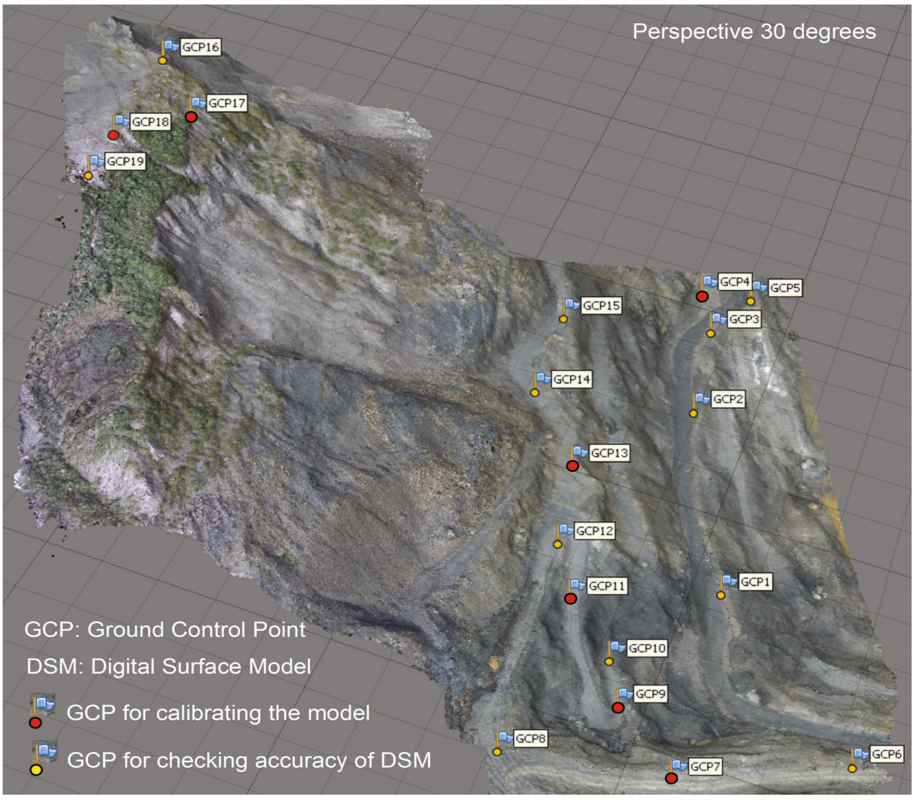

Fig. 5. 3D dense cloud and distribution of the GCPs in the study area.

Using the obtained coefficients, a 3-D dense cloud (Fig. 5) and a Digital Surface Model (DSM) (Fig. 6) for the study area were generated. Based on the DSM, a slope map (Fig. 7) was generated additionally. The goodness-of-fit of the DSM model with the calibrating dataset is shown in Table 5. It could be seen that RMSE for X, Y, Z, XY, XYZ is 1.1 cm, 1.9 cm, 0.8 cm, 2.2 cm, and 2.3 cm, respectively. The highest error for X is 2.9 cm and for Y is 3.1 cm (GCP1, Table 5). Whereas the highest error for Z is 1.7 cm (GCP14, Table 5) and the highest error for XY and XYZ are both 4.3 cm (GCPs 1 and 2, Table 5). These indicate that the fit of the DSM model with the calibrating dataset is very high.

Table 5. Error and RMSE in X, Y, Z, XY, and XYZ of GCPs used for the model calibration.

Calibration points	X error (m)	Y error (m)	Z error (m)	XY error (m)	XYZ error (m)
GCP1	0.029	0.031	−0.007	0.043	0.043
GCP2	−0.013	−0.041	−0.004	0.043	0.043
GCP3	0.009	0.025	0.004	0.026	0.027
GCP5	−0.006	−0.009	0.001	0.011	0.011
GCP6	−0.005	−0.009	0.002	0.010	0.011
GCP8	−0.005	−0.005	−0.012	0.007	0.014
GCP10	−0.013	0.017	0.007	0.022	0.023
GCP12	0.005	−0.024	0.008	0.024	0.025
GCP14	−0.002	−0.001	−0.017	0.002	0.017
GCP15	−0.005	0.009	0.012	0.011	0.016
GCP16	−0.002	0.001	−0.003	0.002	0.004
GCP19	0.002	0.001	0.000	0.002	0.002
RMSE	0.011	0.019	0.008	0.022	0.023

Since the calibrating dataset was used for both the optimization process and the goodness-of-fit, the result may be too positive. Therefore, the checking dataset that was not used in the calibration phase was used to assess the accuracy of the DSM model. The result is shown in Table 6. It could be seen that RMSE for X, Y, Z, XY, XYZ is 1.8 cm, 2.4 cm, 3.2 cm, 3.0 cm, and 4.4 cm, respectively. The highest error for X is 2.9 cm (GCP18), for Y is 4.4 cm (GCP7), for Z is 8.1 cm (GCP7), for XY is 4.9 cm (GCP18), and for XYZ is 9.2 cm (GCP7). These indicate that the accuracy of the DSM model is very high with the checked GCPs at hand.

Interpretation of the DSM model of the study area shows a complex topography. The maximum and minimum elevations are 137.5 m and −90.9 m, respectively. The difference between the highest point and the lowest point of the DSM model is 228.4 m (Fig. 6), whereas the mean and the standard deviation are 20.3 m and 64.3 m. For case of the slope map (Fig. 7) that was generated from the DSM, the maximum and the minimum slopes are 84.3° and 0.1°, respectively, whereas the mean and the standard deviations of the map are 25.4° and 14.7°, respectively.

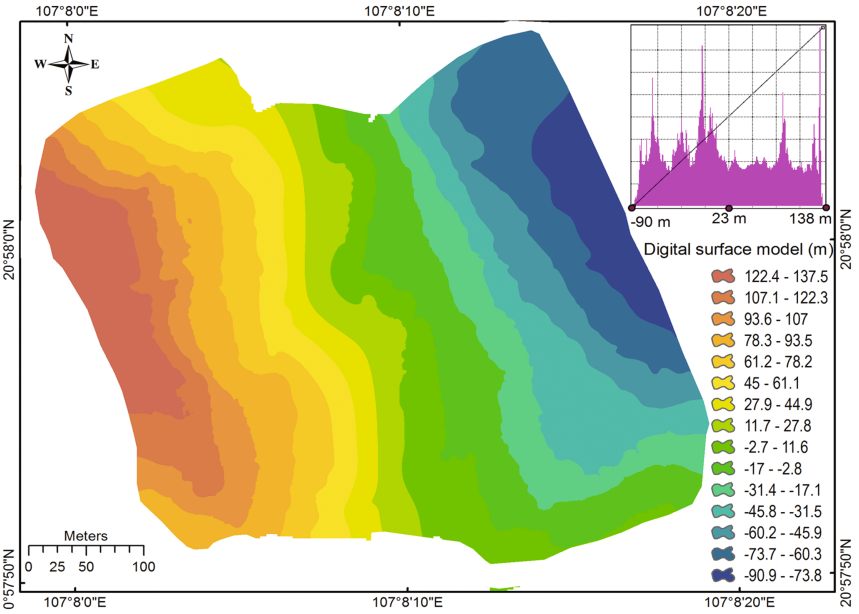

Fig. 6. Digital Surface Model (DSM) for the study area.

Table 6. Error and RMSE in X, Y, Z, XY, and XYZ of check points in this project.

Check points	X error (m)	Y error (m)	Z error (m)	XY error (m)	XYZ error (m)
GCP4	−0.010	−0.006	−0.021	0.012	0.024
GCP7	0.001	0.044	0.081	0.044	0.092
GCP9	−0.025	0.014	0.000	0.029	0.029
GCP11	0.012	0.017	−0.007	0.021	0.022
GCP13	−0.021	0.009	0.016	0.023	0.028
GCP17	0.004	0.001	0.002	0.004	0.005
GCP18	−0.029	0.040	0.002	0.049	0.049
RMSE	0.018	0.024	0.032	0.030	0.044

3.2 Influence of Ground Control Point and Its Distribution to the Accuracy of the DSM Model

To assess the influence of GCPs and its distribution to the accuracy of the DSM model, we varied the number of GCPs used for the calibration (camera-lens optimization and bundle block adjustment) and generated difference DSMs for this study area using the same captured images. Accordingly, six test cases were considered: Case 1, 3GCPs was selected among the 19 GCPs and used for the calibration (CAL), whereas the remaining 16 GCPs were used for the checking accuracy (CHC) of the resulting DSM; Case 2 with 5GCPs for CAL and 14 GCPs for CHC; Case 3 with 7 GCPs for CAL and 12 GCPs for CHC; Case 4 with 9 GCPs for CAL and 10 GCPs for CHC; Case 5 with 11

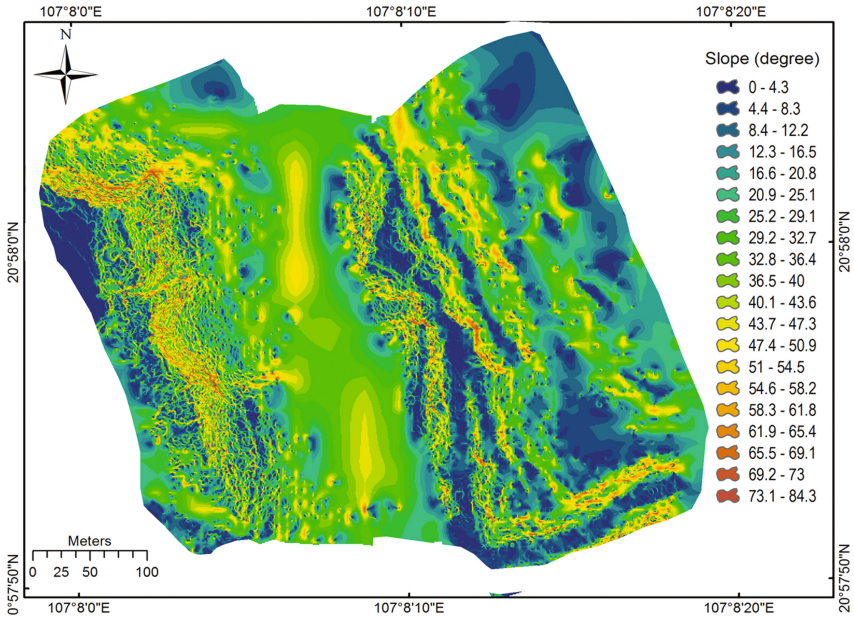

Fig. 7. Slope map generated from the DSM model for the study area.

GCPs for CAL and 10 GCPs for CHC; and Case 6 with 13 GCPs for CAL and 6 GCPs for CHC. The detailed GCPs used for CAL and CHS are shown in Table 7.

The detailed results of the accuracy of these DSMs are shown in Table 7 and errors of GCPs used in these DSMs are shown in Fig. 8. It could be observed that the goodness-of-fit of the DSM decreased when more GCPs were added to the CAL process. $RMSE_{XY}$ and $RMSE_{XYZ}$ are 0.005 m and 0.008, respectively, at Case 1 are increased to 0.021 m and 0.022 m, respectively, in Case 6. In addition, detailed errors

Table 7. RMSE (m) in X, Y, Z, XY, and XYZ of check points in this project (CAL: calibration; CHC: Checking; GCP: Ground control point).

Case	Task	$RMSE_X$	$RMSE_Y$	$RMSE_Z$	$RMSE_{XY}$	$RMSE_{XYZ}$	GCPused
1	CAL	0.001	0.005	0.006	0.005	0.008	3 GCPs:5,6,18
	CHC	0.785	0.597	0.911	0.986	1.343	16 GCPs:1-4,7-17,19
2	CAL	0.003	0.010	0.012	0.010	0.016	5 GCPs: 5,6,8,15,18
	CHC	0.139	0.212	0.497	0.253	0.558	14 GCPs:1-4,7,9-14,16,17,19
3	CAL	0.008	0.007	0.006	0.010	0.012	7 GCPs: 4,7,9,11,13,17,18
	CHC	0.075	0.175	0.291	0.190	0.348	12 GCPs: 1-3,5-7,8,10,12,14-16,19
4	CAL	0.006	0.014	0.006	0.016	0.017	9 GCPs: 1,2,5,6,8,12,15,16,19
	CHC	0.038	0.111	0.216	0.117	0.246	10 GCPs: 3,4,7,9-11,13,14,17,18
5	CAL	0.008	0.014	0.008	0.016	0.018	11 GCPs: 1,2,5,6,7,8,11,14,15,16,19
	CHC	0.038	0.060	0.051	0.071	0.088	8 GCPs: 3,4, 9,10,12,13, 17,18
6	CAL	0.013	0.016	0.007	0.021	0.022	13 GCPs: 1-3,5-9,11,14,15,16,19
	CHC	0.030	0.029	0.047	0.042	0.063	6 GCPs: 4,10,12,13, 17,18

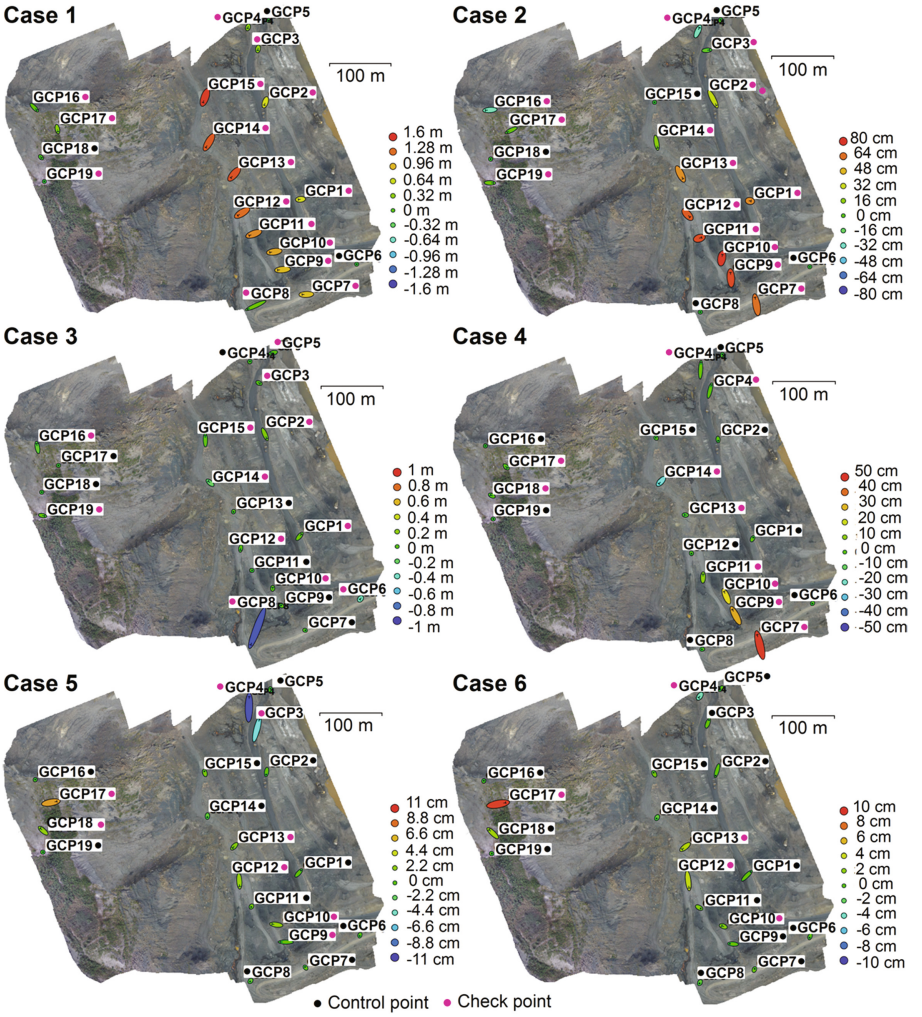

Fig. 8. Estimated errors of the calibrated GCPs and checked GCPs in the six testing cases in this study, in which Z error is represented by ellipse color, whereas X,Y errors are represented by ellipse shape.

in Z and XY components is shown in Fig. 8, in which ellipse color represents Z error, whereas ellipse shape represents for X,Y errors.

The checking results (Table 7) show that the accuracy of the DSM model is increased significantly, when more GCPs were added to the model. Specifically, RMSE in the Case 1 (Table 7, Fig. 8) for X (0.785 m), Y (0.579 m), Z (0.911 m), XY (0.986 m), and XYZ (1.343 m) significantly decreased in the Case 6, where RMSE for X, Y, Z, XY, and XYZ is 0.030 m, 0.029 m, 0.047 m, 0.042 m, and 0.063 m, respectively (Table 7, Fig. 8). This finding is in agreement with Tahar [25] and

Agüera-Vega et al. [24] who concluded that accuracy of the DSM increased when more GCPs were used in the bundle block adjustment.

4 Concluding Remarks

This research assesses potential application of small UAV, SfM photogrammetry for generating DSM and its accuracy assessment at open-pit coal mine area with a case study at the Nui Beo coal mine, Quang Ninh province, one of the largest open-pit coal mines in Vietnam. Accordingly, a lightweight and low-cost DJI Phantom 3 Professional equipped by the nonmetric RGB Sony EXMOR camera was used. A total of 206 images were captured, and in addition, 19 GCPs were established and determined XYZ coordination (VN2000/UTM Zone 48 N) using a Leica TS09 total station (1”angular accuracy and 1.5 mm + 2 ppm distance accuracy).

The result showed that the DSM model has high accuracy; RMSE in the calibrating dataset is 0.8 cm and 2.2 cm for vertical and horizontal, respectively indicating high success-rate of fit, whereas RMSE in the checking dataset is 3.2 cm and 3.0 cm for vertical and horizontal, indicating high accuracy. These indicate that the processes of capturing images, establishment of GCPs, and photogrammetric processing were carried out successfully.

Overall, one of the most interested issues in using UAV and SfM photogrammetry is how to increase the horizontal and vertical accuracy of UAV products. According to Agüera-Vega et al. [24], flight altitude and number of GCPs influences vertical accuracy significantly but not terrain morphology, whereas horizontal accuracy is not effected by flight altitude and terrain morphology. However, the optimal number of GCPs for a study area still is a questionable matter. Literature review shows that most studies only reported number of GCPs used without documenting the background used. To our knowledge, few works have investigated the correlation of number of GCPs and DSM accuracy with different conclusions, i.e. Tahar [25] and Agüera-Vega et al. [24] concluded that the number of GCP influence the horizontal accuracy of the DSM model significantly, whereas Mancini et al. [26] reported that decreasing the number of GCPs does not influence the accuracy of the DSM. The result in this study (Fig. 8 and Table 7) shows a different result compared to [26], where the horizontal and vertical errors were significantly reduced when more GCPs were added to the model.

A limitation of this research is related to the distribution of the GCPs, it could be observed that the central and low left corner areas have no GCP; therefore accuracy of the DSM model for these areas was not assessed. It is noted that these are unsafety areas for us to research and establish GCPs because the coal seams in these area were exploiting. Despite the limitation, based on the finding in this research, it could be concluded that small UAV and SfM photogrammetry are valid and efficient tools for topographic mapping at complex terrain areas such as open-pit coal mine.

Conflict of interest. The authors declare that there is no conflict of interest.

Acknowledgement. This research was supported by Department of Mine Surveying, Faculty of Geomatics and Land Administration, Hanoi University of Mining and Geology (Vietnam) and the Nui Beo coal joint stock company - VINACOMIN group.

References

1. Ogundare, J.O.: Precision Surveying: The Principles and Geomatics Practice. Wiley, Hoboken (2015)
2. Siebert, S., Teizer, J.: Mobile 3D mapping for surveying earthwork projects using an Unmanned Aerial Vehicle (UAV) system. Autom. Constr. **41**, 1–14 (2014)
3. Hugenholtz, C.H., Walker, J., Brown, O., Myshak, S.: Earthwork volumetrics with an unmanned aerial vehicle and softcopy photogrammetry. J. Surveying Eng. **141**, 06014003 (2014)
4. Carrivick, J.L., Smith, M.W., Quincey, D.J.: Structure From Motion in the Geosciences. Wiley, Handbook (2016)
5. Fernández-Hernandez, J., González-Aguilera, D., Rodríguez-Gonzálvez, P., Mancera-Taboada, J.: Image-based modelling from Unmanned Aerial Vehicle (UAV) photogrammetry: an effective. Low-Cost Tool Archaeol. Appl. Archaeometry **57**, 128–145 (2015)
6. Vasuki, Y., Holden, E.-J., Kovesi, P., Micklethwaite, S.: Semi-automatic mapping of geological structures using UAV-based photogrammetric data: an image analysis approach. Comput. Geosci. **69**, 22–32 (2014)
7. Cryderman, C., Mah, S.B., Shufletoski, A.: Evaluation of UAV photogrammetric accuracy for mapping and earthworks computations. Geomatica **68**, 309–317 (2014)
8. Clapuyt, F., Vanacker, V., Van Oost, K.: Reproducibility of UAV-based earth topography reconstructions based on Structure-from-Motion algorithms. Geomorphology **260**, 4–15 (2016)
9. Shahbazi, M., Sohn, G., Théau, J., Menard, P.: Development and evaluation of a UAV-photogrammetry system for precise 3D environmental modeling. Sensors **15**, 27493–27524 (2015)
10. Tonkin, T.N., Midgley, N., Cook, S.J., Graham, D.J.: Ice-cored moraine degradation mapped and quantified using an unmanned aerial vehicle: a case study from a polythermal glacier in Svalbard. Geomorphology **258**, 1–10 (2016)
11. Eltner, A., Baumgart, P., Maas, H.G., Faust, D.: Multi-temporal UAV data for automatic measurement of rill and interrill erosion on loess soil. Earth Surf. Proc. Land. **40**, 741–755 (2015)
12. Candiago, S., Remondino, F., De Giglio, M., Dubbini, M., Gattelli, M.: Evaluating multispectral images and vegetation indices for precision farming applications from UAV images. Remote Sens. **7**, 4026–4047 (2015)
13. Hugenholtz, C.H., Whitehead, K., Brown, O.W., Barchyn, T.E., Moorman, B.J., LeClair, A., Riddell, K., Hamilton, T.: Geomorphological mapping with a small unmanned aircraft system (sUAS): feature detection and accuracy assessment of a photogrammetrically-derived digital terrain model. Geomorphology **194**, 16–24 (2013)
14. Tuan, V.A.: Annual report of the Nui Beo coal joint stock company - VINACOMIN group. The Nui Beo coal joint stock compan (2013)
15. Nui Beo Joint Stock company: The environmental impact assessent report on the project of investments and construction of underground mining of the Nui Beo coal mine (2013)

16. Ajayi, O.G., Salubi, A.A., Angbas, A.F., Odigure, M.G.: Generation of accurate digital elevation models from UAV acquired low percentage overlapping images. Int. J. Remote Sens. **38**, 3113–3134 (2017)
17. Han, Y.-G., Jung, S.-H., Kwon, O.: How to utilize vegetation survey using drone image and image analysis software. J. Ecol. Environ. **41**, 18 (2017)
18. Tien Bui, D., Tran, C.T., Pradhan, B., Revhaug, I., Seidu, R.: iGeoTrans – a novel iOS application for GPS positioning in geosciences. Geocarto Int. (2014)
19. Sona, G., Pinto, L., Pagliari, D., Passoni, D., Gini, R.: Experimental analysis of different software packages for orientation and digital surface modelling from UAV images. Earth Sci. Inf. **7**, 97–107 (2014)
20. Leon, J.X., Roelfsema, C.M., Saunders, M.I., Phinn, S.R.: Measuring coral reef terrain roughness using 'Structure-from-Motion'close-range photogrammetry. Geomorphology **242**, 21–28 (2015)
21. Lowe, D.G.: Distinctive image features from scale-invariant keypoints. Int. J. Comput. Vision **60**, 91–110 (2004)
22. Fryer, J.G., Brown, D.C.: Lens distortion for close-range photogrammetry. Photogrammetric Eng. Remote Sens. **52**, 51–58 (1986)
23. Manual, A.P.U.: Professional Edition, Version 1.2. Russia: Agisoft LLC (2016)
24. Agüera-Vega, F., Carvajal-Ramírez, F., Martínez-Carricondo, P.: Accuracy of digital surface models and orthophotos derived from unmanned aerial vehicle photogrammetry. J. Surveying Eng. (2016). 04016025
25. Tahar, K.: An evaluation on different number of ground control points in unmanned aerial vehicle photogrammetric block. ISPRS J. Photogramm. XL-2 (W2) 93–98 (2013)
26. Mancini, F., Dubbini, M., Gattelli, M., Stecchi, F., Fabbri, S., Gabbianelli, G.: Using unmanned aerial vehicles (UAV) for high-resolution reconstruction of topography: the structure from motion approach on coastal environments. Remote Sens. **5**, 6880–6898 (2013)

http://www.springer.com/978-3-319-68239-6

Advances and Applications in Geospatial Technology and Earth Resources
Proceedings of the International Conference on Geo-Spatial Technologies and Earth Resources 2017
Tien Bui, D.; Ngoc Do, A.; Bui, H.-B.; Hoang, N.-D. (Eds.)
2018, XI, 396 p. 197 illus., Hardcover
ISBN: 978-3-319-68239-6